

Néel Ordered Magnetic Phases in Bipartite Quasicrystals

Jia-Heng Ji,^{1,*} Zhi-Yan Shao,^{1,*} Yu-Bo Liu,^{2,*} and Fan Yang^{1,†}

¹*School of Physics, Beijing Institute of Technology, Beijing 100081, China*

²*Institute of Theoretical Physics, Chinese Academic of Science, Beijing 100080, China*

Magnetism is a fundamental research area in which the recently proposed altermagnetism (AM) has become an emergent frontier. Very recently, the quasicrystal (QC) was proposed as a possible platform to realize AM. However, the existence of AM in QCs still lacks vigorous evidence. In this work, we adopt the sign-problem-free projector quantum Monte Carlo (PQMC) algorithm to investigate the magnetic phases in the half-filled Hubbard models in various 2D bipartite QCs, and always obtain Néel ordered states. While the Néel states in bipartite crystals are usually antiferromagnetism (AFM), we find it common that those in bipartite QCs can also be AM or ferromagnetism (FM). Based on symmetry analysis, combined with our comprehensive PQMC results, we propose a general criterion for determining the magnetism classes of the Néel states in a bipartite QC: According to whether the two sublattices are related by the inversion, the other point-group operation, or no operation about the unique symmetry center in the QC, the corresponding Néel state is AFM, AM or FM, respectively. For example, our results yield AM for the two D_4 -symmetric Thue-Morse QCs and FM for the D_5 -symmetric Penrose QC at half-filling. Our results provide a solid foundation for experimental investigations and potential applications of different classes of magnetism in QCs.

Introduction. — Magnetism plays a crucial role in condensed matter physics, with ferromagnetism (FM) and antiferromagnetism (AFM) representing two traditional magnetic phases. The representative physical origins of FM include the Stoner criterion[1] that considers direct exchange interactions between itinerant electrons and the double-exchange mechanism[2, 3] that describes interactions of itinerant electrons with localized spins. In contrast, AFM usually emerges through Fermi surface nesting[4–6] in weak-coupling systems or superexchange interactions[7–10] in strong-coupling systems. Composite lattice structures can further induce ferrimagnetism (FIM) by the superexchange mechanism[11], which is a subtype of FM with opposite magnetic moments of unequal magnitude on distinct sublattices yielding residual net magnetization.

Recently, altermagnetism (AM) has been considered as a distinct class of magnetic phase[12–25], characterized by zero net magnetism similar to AFM and spin-split electronic band structures similar to FM. Theoretically, AM can be realized by various mechanisms, e.g. the presence of nonmagnetic atoms[26, 27], spontaneously broken orbital order[28–30], Pomeranchuk instabilities[31–34] or spin-cluster engineering[35]. Currently, although there exist experimental evidences to support that some materials are possible candidates for AM [36–48], the confirmed ones among them are still rare.

To explore more possibilities to realize AM, researchers recently considered AM in quasicrystals (QCs) [49–51]. The QC is an aperiodic structure that possesses long-range-order, in which the higher-fold rotational symmetries and the absence of translational symmetry[52–54] produce various novel phases[49–51, 55–86], including the magnetic phases[49–51, 55, 57, 59, 60, 64, 74, 75, 83]. In Refs.[49, 50], the possibility of realizing AM in some 2D QCs is proposed through mean-field (MF) studies. In

Ref.[51], it is pointed out that without the translational symmetry to recover the broken parity (\mathcal{P}) and time-reversal (\mathcal{T}) symmetry, point-group symmetries other than \mathcal{P} can protect AM, making AM more common in QCs than in crystals. Furthermore, since a QC can host at most one inversion center, magnetic phases can be easily classified according to the irreducible representations (IRRs) of the point-group[51]. Ref.[51] points out that nearly half of the 1D IRRs correspond to AM, implying the widespread presence of AM in QCs.

However, the existence of AM in QCs still lacks rigorous evidence. On the one hand, the possible realization of AM in QCs investigated by self-consistent MF approach is not persuasive: Firstly, the MF theory cannot capture the quantum fluctuations. Secondly, due to absence of translational symmetry, it is difficult to determine the spatial distribution pattern of the magnetic moments in QCs, easily leading to being trapped at local energy minima. On the other hand, although the classification[51] indicates which IRRs correspond to AM, it is not easy to determine which IRRP the ground state of a given QC belongs to. To address these problems, we employ the sign-problem-free projector quantum Monte Carlo (PQMC) algorithm[87–89] to study the magnetic phases in bipartite QCs by solving the half-filled large- U Hubbard model, which turn out to be Néel-ordered states. Intriguingly, in contrast to the cases in bipartite crystals wherein the Néel states are usually AFM, the Néel states in QCs can be AFM, AM or FM, determined by symmetries of the QCs.

In this work, we investigate the magnetic phases in the half-filled large- U Hubbard models in various 2D bipartite QCs, which are expected to be Néel ordered phases. We propose a general criterion for determining the magnetism classes of the Néel states in these bipartite QCs: Due to lack of translational symmetry, there exists one

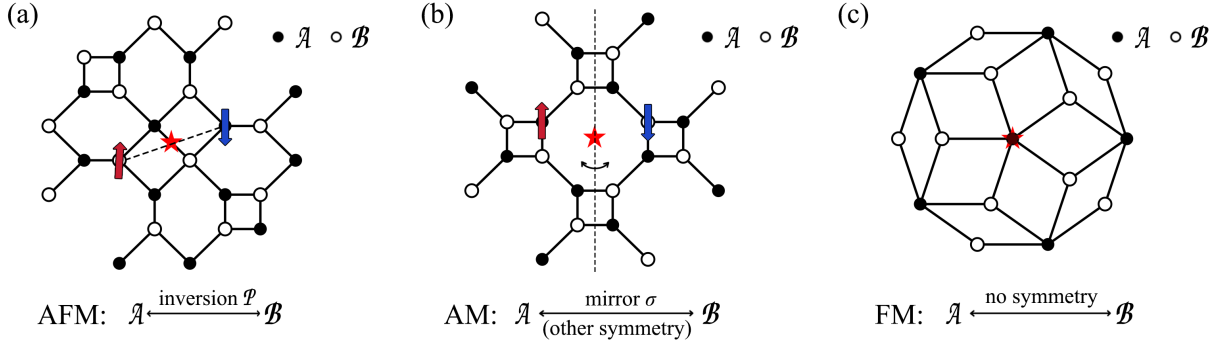


FIG. 1. Schematic diagrams of the lattice geometry-based criterion for determining the magnetic classes of Néel ordered states in bipartite QCs. (a) Néel ordered AFM is allowed in, e.g. the D_2 -symmetric Thue-Morse QC, whose two sublattices are related by \mathcal{P} . A pair of sites related by \mathcal{P} (dashed line) with opposite magnetic moments (red up arrow for spin-up and blue down arrow for spin-down) are marked in (a). (b) Néel ordered AM emerges in, e.g. the D_4 -symmetric Thue-Morse QC, where other symmetry operation (e.g., the mirror σ) instead of \mathcal{P} connects the two sublattices. The dashed line represents a mirror axis. The red (blue) arrow indicates the same meaning as in (a). (c) Néel ordered FM is present in, e.g. the D_5 -symmetric Penrose QC, in which no symmetry operations relate the two sublattices. In (a-c), the red stars label the symmetry centers, and the solid (hollow) circles denote the sites in sublattice \mathcal{A} (\mathcal{B}) and the solid lines represent the NN or NNN bonds.

unique point-group symmetry center in a QC. According to whether the two sublattices are related by the inversion operation \mathcal{P} , the other point-group operation, or no operation about this symmetry center, the corresponding Néel state is AFM, AM or FM, respectively. For verification, we solve the ground state via the sign-problem-free PQMC algorithm to determine the magnetic pattern and study the spectroscopic properties. This PQMC simulation verifies our criterion and reveals the robust existence of AM, FM and AFM Néel orders in bipartite QCs, providing a theoretical foundation for future experimental investigations and potential applications.

Model and Approach. — As the beginning of our study, we construct the Hubbard model in QCs as

$$H = H_{\text{TB}} + U \sum_i n_{i\uparrow} n_{i\downarrow}, \quad (1)$$

where $n_{i\sigma}$ is the particle number of spin- σ at site i and H_{TB} represents the tight-binding (TB) Hamiltonian, including up to the nearest neighbor (NN) or the next nearest neighbor (NNN) inter-sublattice hoppings. We set the hopping integral along the NN bonds t_1 as an energy unit and $U = 4t_1$ throughout this work.

The Hamiltonian (1) is solved by the PQMC algorithm, in which the expectation of a physical quantity O is

$$\langle O \rangle = \lim_{\Theta \rightarrow \infty} \frac{\langle \psi | e^{-\Theta H} O e^{-\Theta H} | \psi \rangle}{\langle \psi | e^{-2\Theta H} | \psi \rangle}, \quad (2)$$

where $|\psi\rangle$ represents the trial wave function, and Θ is the total imaginary time. This PQMC algorithm is sign-problem-free for the half-filled case in bipartite QCs.

Traditionally, the total imaginary time projection operator $e^{-\Theta H}$ is decomposed as $e^{-\Theta H} = e^{-n\Delta\tau H}$ with a uniform time slice $\Delta\tau = \Theta/n$. Here we adopt a non-

uniform time-slice strategy to decompose $e^{-\Theta H}$ as

$$e^{-\Theta H} = \lim_{n \rightarrow \infty} e^{-\Delta\tau_1 H} e^{-\Delta\tau_2 H} \dots e^{-\Delta\tau_n H}, \quad (3)$$

with $\Theta = \sum_{i=1}^n \Delta\tau_i$ and

$$\Delta\tau_1 \geq \Delta\tau_2 \geq \dots \geq \Delta\tau_n > 0. \quad (4)$$

Our tests in small clusters suggest that this strategy can effectively balance the number of time slice and the Trotter error, and thus efficiently accelerate the simulation. See more details in Supplementary Material (SM)[90].

In the PQMC simulations, we apply two kinds of trial wave functions. The first trial wave function reads

$$|\psi\rangle = \prod_{m=1}^N \sum_{i=1}^N \phi_{im} (c_{i\uparrow}^\dagger + c_{i\downarrow}^\dagger) |0\rangle, \quad (5)$$

where $c_{i\sigma}^\dagger$ creates a spin- σ electron at site i and N denotes the site number. ϕ_{im} is the single-particle wave function at site i for the m -th eigen state of H_{TB} and $|0\rangle$ represents the Fock vacuum. We adopt this trial wave function when the total magnetism of the ground state is unknown, e.g. in the FM phase. The second trial wave function is

$$|\psi\rangle = \prod_{m=1}^{N/2} \prod_{\sigma} \sum_{i=1}^N \phi_{im} c_{i\sigma}^\dagger |0\rangle. \quad (6)$$

In Eq. (6), the total magnetism is fixed at zero. Therefore, in the cases of AFM or AM ground states, adopting this trial wave function turns out to accelerate convergence. See more details in the SM[90].

Magnetic classes of Néel orders in bipartite QCs. — For large- U , the two sublattices within a bipartite lattice tend to host magnetic moments with opposite orientations, which constitute the Néel order, so that the energy

of the low-energy effective superexchange interaction between the two sublattices is minimized. However, this does not ensure a zero net magnetism in QCs: Firstly, the inevitable quantum fluctuations lead to partial polarization in each sublattice. Secondly, different sites within a QC reside in distinct local environments and experience different quantum fluctuation strengths, and thus host different magnitudes of magnetic moment, unless they are related by any point-group operation. Therefore, in a bipartite QC, based on whether the two sublattices are related by any point-group symmetry element and by which symmetry, there exist three possibilities.

The first is the Néel ordered AFM. If the two sublattices are related by \mathcal{P} , as shown in Fig. 1 (a), each pair of sites related by \mathcal{P} must belong to different sublattices, and will thus accommodate magnetic moments with equal magnitudes but opposite orientations. Therefore, the global magnetic pattern will be flipped after \mathcal{P} , which can be recovered after an extra \mathcal{T} operation, leading to the combined \mathcal{PT} symmetric AFM phase.

The second is the Néel ordered AM. If the two sublattices are not related by \mathcal{P} , but are related by an alternative point-group symmetry, e.g. the mirror σ , as illustrated in Fig. 1 (b), this symmetry can also ensure zero net magnetism. In this case, the Néel state lacks the \mathcal{PT} symmetry, leading to a Néel ordered AM. Note that this differs from the situation in crystals. For example, in a square lattice, although the two sublattices cannot be related by a plaquette-centered \mathcal{P} operation, like that illustrated in Fig. 1 (b), they can alternatively be related by a bond-centered \mathcal{P} operation, leading to a \mathcal{PT} symmetric AFM Néel state. However, in QCs, due to the absence of translational symmetry, there can exist at most one inversion center [51] as marked in Fig. 1(b), which relates one sublattice to itself by \mathcal{P} , leading to the \mathcal{PT} symmetry broken Néel ordered AM phase.

The third is the Néel ordered FM. If there is no point-group symmetry that relates the two sublattices, as shown in Fig. 1 (c), any site in one sublattice transfers to another site in the same sublattice after any symmetry operation (e.g., \mathcal{P} , σ or rotation). In this case, no symmetry ensures the zero net magnetism, and the corresponding Néel state is generally FM phase.

In summary, we have: In a bipartite QC, depending on whether the two sublattices are related by the \mathcal{P} operation, the other point-group operation, or no symmetry operation about the unique symmetry center, the corresponding Néel order is AFM, AM, or FM, respectively.

To verify this proposal, we employ the sign-problem-free PQMC approach to study the half-filled large- U Hubbard models in various bipartite QCs as examples.

Examples. — Firstly, we explore the possibility of Néel ordered AM in bipartite QCs. According to the above proposal, this requires that the two sublattices are connected by point-group operations other than \mathcal{P} . The

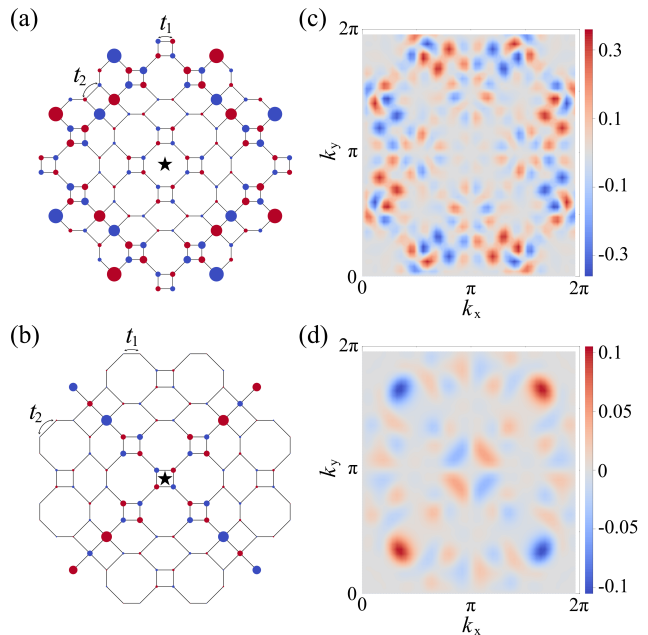


FIG. 2. (a, b) The distribution of the magnetic moments in the D_4 -symmetric Thue-Morse lattice hosting (a) 120 sites with the central 8-site cluster, and (b) 104 sites with the central 4-site cluster. In (a-b), the red (blue) dots represent spin- \uparrow (\downarrow), and the size of each dot represents magnitude of the magnetic moment. The central black stars label the symmetry center and the solid lines with t_1 and t_2 represent the NN and NNN hoppings. (c, d) The spin-resolved spectral density difference $\mathcal{A}_\uparrow(\mathbf{p}, \omega) - \mathcal{A}_\downarrow(\mathbf{p}, \omega)$ as a function of momentum \mathbf{p} for (c) the lattice exhibited in (a) with $\omega = -0.33t_1$, and (d) the lattice exhibited in (b) with $\omega = -0.2t_1$.

two different D_4 -symmetric Thue-Morse lattices shown in Figs. 2 (a) and (b) satisfy this condition: In both QCs, the two sublattices are related by mirror or rotation operation instead of \mathcal{P} . In the following, we verify the existence of Néel ordered AM in the two QCs by the sign-problem-free PQMC approach.

The TB Hamiltonians on the two Thue-Morse lattices include hopping terms along the NN- (t_1) and the NNN (t_2) bonds, as indicated in Figs. 2 (a) and (b) by the solid lines. The magnetic patterns on the two lattices obtained by PQMC are shown in Figs. 2 (a) and (b), which illustrate the Néel orders with opposite spin orientations in the two sublattices. The magnetic pattern shown in Fig. 2 (a) exhibits a $d_{x^2-y^2} \cdot d_{xy}$ -wave symmetry under the D_4 point-group around the symmetry center marked by the solid pentagram: It is unchanged under \mathcal{P} or the rotation c_4^1 and changes sign under the mirror reflection about the four axes of symmetry. The magnetic pattern shown in Fig. 2 (b) exhibits a d_{xy} -wave symmetry: It is unchanged under \mathcal{P} or mirror reflection about the diagonal directions and changes signs under c_4^1 or mirror reflection about the x - or y -axes.

The above two Néel states shown in Fig. 2 remain un-

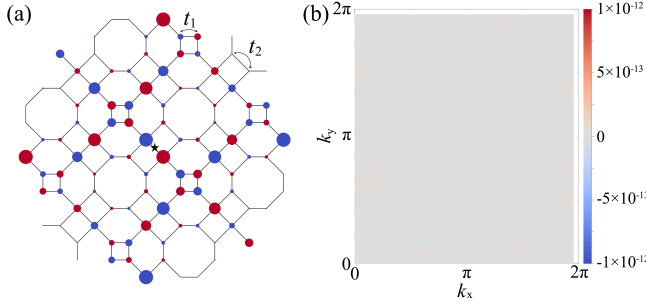


FIG. 3. (a) The distribution of the magnetic moment in the 104-site D_2 -symmetric Thue-Morse lattice. (b) The spin-resolved spectral density difference $\mathcal{A}_\uparrow(\mathbf{p}, \omega) - \mathcal{A}_\downarrow(\mathbf{p}, \omega)$ as a function of momentum \mathbf{p} for arbitrary ω .

changed under \mathcal{P} and then flip spins after an extra \mathcal{T} operation, which break the \mathcal{PT} symmetry and are thus AM. To further characterize AM in QCs, we calculate the spin-resolved angle-resolved photoemission spectrum $\mathcal{A}_{\uparrow, \downarrow}(\mathbf{p}, \omega)$ [49, 50, 91] (see SM[90] for details), which indicates the spectrum weight for spin- \uparrow or \downarrow at a certain energy level ω to detect momentum \mathbf{p} . As shown in Figs. 2 (c) and (d), the spectrum differences $\mathcal{A}_\uparrow(\mathbf{p}, \omega) - \mathcal{A}_\downarrow(\mathbf{p}, \omega)$ as functions of \mathbf{p} exhibit non-zero value with corresponding symmetries, characterizing AM.

These examples demonstrate the great potential of the QC as a platform to realize AM. Note that the magnetic pattern shown in Fig. 2 (b) exhibits the same d_{xy} -wave symmetry as that in the square-lattice Néel state. In the latter state, the plaquette-centered \mathcal{PT} symmetry is also broken, like that illustrated in Fig. 2 (b). However, the broken \mathcal{PT} symmetry can be recovered after a subsequent translation by a unit vector. Here in the QC, the lack of translational symmetry prevents recovery of the \mathcal{PT} symmetry, making AM more easily realized.

Secondly, we consider the possibility of Néel ordered AFM in bipartite QCs. According to our proposal, this requires that the two sublattices are connected by \mathcal{P} . A typical example is the D_2 -symmetric Thue-Morse lattice shown in Fig. 3 (a), in which the two sublattices are indeed related by \mathcal{P} . The magnetic pattern on this lattice obtained by our PQMC calculation is shown in Fig. 3 (a), which exhibits a Néel order with opposite spin orientations in the two sublattices. This pattern exhibits the p_{x-y} -wave symmetry under the D_2 point-group: It is unchanged under the mirror reflection about the $x + y = 0$ line and changes sign under \mathcal{P} , c_2^1 rotation or mirror reflection about the $x - y = 0$ line. Obviously, such a magnetic pattern would be flipped under \mathcal{P} and recovered after a subsequent \mathcal{T} operation, belonging to the \mathcal{PT} -symmetric AFM phase. The spectrum difference $\mathcal{A}_\uparrow(\mathbf{p}, \omega) - \mathcal{A}_\downarrow(\mathbf{p}, \omega)$ shown in Fig. 3 (b) illustrates zero value for arbitrary (\mathbf{p}, ω) , characterizing AFM.

Finally, we study the possibility of Néel ordered FM in bipartite QCs. According to our proposal, this re-

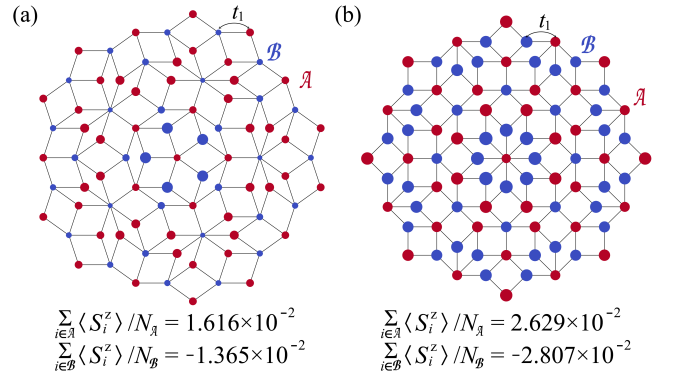


FIG. 4. The distribution of the magnetic moments in (a) the 86-site D_5 -symmetric Penrose lattice, and (b) the 89-site D_8 -symmetric Ammann-Beenker lattice. The average magnetic moment per site for each sublattice is shown in each figure.

quires that the two sublattices cannot be related by any point-group operation. A class of bipartite lattices which satisfy this condition is those with a single central site as the symmetry center, which is never related to another site by any point-group operation. The D_5 -symmetric Penrose lattice and the D_8 -symmetric Ammann-Beenker lattice shown in Figs. 4 (a) and (b) belong to this class.

The TB Hamiltonians on the two lattices include only the NN hoppings, as indicated in Figs. 4 (a, b) by the solid lines, wherein the magnetic patterns obtained by our PQMC calculations are shown. Both magnetic patterns illustrate Néel orders, and exhibit the s -wave symmetry, as they are unchanged under all point-group operations. Without protection by symmetry, the magnitudes of the average magnetic moments per site in the two sublattices are not equal, as provided in Figs. 4 (a) and (b). Since the two sublattices host equal site numbers in the thermal dynamic limit, the net magnetism is non-zero, resulting in FM. This Néel ordered FM originates from the unequivalence between the two sublattices in this type of bipartite QCs, similar to the FIM in crystals.

Conclusion and Discussion. — We have investigated the magnetic phases in half-filled large- U Hubbard models in various bipartite QCs, demonstrating the feasibility of QC as a symmetry-protected platform to realize AM, AFM and FM. Based on symmetry analysis, combined with our comprehensive PQMC results, we propose a general criterion to determine the magnetism classes of the Néel states in bipartite QCs, which brings convenience in the exploration and application of magnetism in QCs.

This work focuses on half-filled Hubbard models with fixed U in bipartite QCs. With tuning U and the doping, more intriguing phases are expected. On the one hand, in the case of weak U , without driving by Fermi surface nesting in QCs, it is fascinating to figure out the emergent magnetic patterns. On the other hand, upon doping, unconventional superconductivity (SC) could emerge. Particularly, the AM or FM fluctuations might mediate

triplet SC[92–108]. These topics are left for future study.

Acknowledgment We are grateful to the stimulating discussions with Cong Zhang. F.Y. is supported by the national natural science foundation of China under the Grant Nos. 12574141, 12234016, 12074031. Y. L. is supported by the postdoctoral innovation talent support program (Grant No. A5B10039).

* These authors contributed equally to this work.

† yangfan.blg@bit.edu.cn

- [1] E. C. Stoner, Collective electron ferromagnetism, *Proceedings of the Royal Society of London. Series A. Mathematical and Physical Sciences* **165**, 372 (1938).
- [2] C. Zener, Interaction between the d -shells in the transition metals. ii. ferromagnetic compounds of manganese with perovskite structure, *Phys. Rev.* **82**, 403 (1951).
- [3] P. G. de Gennes, Effects of double exchange in magnetic crystals, *Phys. Rev.* **118**, 141 (1960).
- [4] E. Fawcett, Spin-density-wave antiferromagnetism in chromium, *Rev. Mod. Phys.* **60**, 209 (1988).
- [5] D. Scalapino, The case for $d_{x^2-y^2}$ pairing in the cuprate superconductors, *Physics Reports* **250**, 329 (1995).
- [6] M. Imada, A. Fujimori, and Y. Tokura, Metal-insulator transitions, *Rev. Mod. Phys.* **70**, 1039 (1998).
- [7] H. Kramers, L'interaction entre les atomes magnétogènes dans un cristal paramagnétique, *Physica* **1**, 182 (1934).
- [8] P. W. Anderson, Antiferromagnetism. theory of superexchange interaction, *Phys. Rev.* **79**, 350 (1950).
- [9] J. B. Goodenough, An interpretation of the magnetic properties of the perovskite-type mixed crystals $\text{La}_{1-x}\text{Sr}_x\text{CoO}_{3-\lambda}$, *Journal of Physics and Chemistry of Solids* **6**, 287 (1958).
- [10] J. Kanamori, Superexchange interaction and symmetry properties of electron orbitals, *Journal of Physics and Chemistry of Solids* **10**, 87 (1959).
- [11] J. B. Goodenough, Theory of the role of covalence in the perovskite-type manganites $[\text{La}, M(\text{II})]\text{MnO}_3$, *Phys. Rev.* **100**, 564 (1955).
- [12] M. Naka, S. Hayami, H. Kusunose, Y. Yanagi, Y. Motome, and H. Seo, Spin current generation in organic antiferromagnets, *Nature Communications* **10**, 4305 (2019).
- [13] K.-H. Ahn, A. Hariki, K.-W. Lee, and J. Kuneš, Antiferromagnetism in RuO_2 as d -wave Pomeranchuk instability, *Phys. Rev. B* **99**, 184432 (2019).
- [14] S. Hayami, Y. Yanagi, and H. Kusunose, Momentum-dependent spin splitting by collinear antiferromagnetic ordering, *J. Phys. Soc. Jpn.* **88**, 123702 (2019).
- [15] L. Šmejkal, R. González-Hernández, T. Jungwirth, and J. Sinova, Crystal time-reversal symmetry breaking and spontaneous Hall effect in collinear antiferromagnets, *Science advances* **6**, eaaz8809 (2020).
- [16] L.-D. Yuan, Z. Wang, J.-W. Luo, E. I. Rashba, and A. Zunger, Giant momentum-dependent spin splitting in centrosymmetric low-Z antiferromagnets, *Phys. Rev. B* **102**, 014422 (2020).
- [17] D.-F. Shao, S.-H. Zhang, M. Li, C.-B. Eom, and E. Y. Tsymlal, Spin-neutral currents for spintronics, *Nat. Commun.* **12**, 7061 (2021).
- [18] I. I. Mazin, K. Koepernik, M. D. Johannes, R. González-Hernández, and L. Šmejkal, Prediction of unconventional magnetism in doped FeSb_2 , *Proc. Natl. Acad. Sci.* **118**, e2108924118 (2021).
- [19] H.-Y. Ma, M. Hu, N. Li, J. Liu, W. Yao, J.-F. Jia, and J. Liu, Multifunctional antiferromagnetic materials with giant piezomagnetism and noncollinear spin current, *Nat. Commun.* **12**, 2846 (2021).
- [20] L.-D. Yuan, Z. Wang, J.-W. Luo, and A. Zunger, Prediction of low-Z collinear and noncollinear antiferromagnetic compounds having momentum-dependent spin splitting even without spin-orbit coupling, *Phys. Rev. Mater.* **5**, 014409 (2021).
- [21] X. Zhou, W. Feng, R.-W. Zhang, L. Šmejkal, J. Sinova, Y. Mokrousov, and Y. Yao, Crystal thermal transport in altermagnetic RuO_2 , *Phys. Rev. Lett.* **132**, 056701 (2024).
- [22] R.-W. Zhang, C. Cui, R. Li, J. Duan, L. Li, Z.-M. Yu, and Y. Yao, Predictable gate-field control of spin in altermagnets with spin-layer coupling, *Phys. Rev. Lett.* **133**, 056401 (2024).
- [23] L. Bai, W. Feng, S. Liu, L. Šmejkal, Y. Mokrousov, and Y. Yao, Altermagnetism: Exploring new frontiers in magnetism and spintronics, *Advanced Functional Materials* **34**, 2409327 (2024).
- [24] L. Han, X. Fu, R. Peng, X. Cheng, J. Dai, L. Liu, Y. Li, Y. Zhang, W. Zhu, H. Bai, Y. Zhou, S. Liang, C. Chen, Q. Wang, X. Chen, L. Yang, Y. Zhang, C. Song, J. Liu, and F. Pan, Electrical 180° switching of Néel vector in spin-splitting antiferromagnet, *Science Advances* **10**, eadn0479 (2024).
- [25] Z. Zhou, X. Cheng, M. Hu, R. Chu, H. Bai, L. Han, J. Liu, F. Pan, and C. Song, Manipulation of the altermagnetic order in CrSb via crystal symmetry, *Nature* **638**, 645 (2025).
- [26] S. S. Fender, O. Gonzalez, and D. K. Bediako, Altermagnetism: A chemical perspective, *Journal of the American Chemical Society* **147**, 2257 (2025).
- [27] L. Šmejkal, J. Sinova, and T. Jungwirth, Beyond conventional ferromagnetism and antiferromagnetism: A phase with nonrelativistic spin and crystal rotation symmetry, *Phys. Rev. X* **12**, 031042 (2022).
- [28] V. Leeb, A. Mook, L. Šmejkal, and J. Knolle, Spontaneous formation of altermagnetism from orbital ordering, *Phys. Rev. Lett.* **132**, 236701 (2024).
- [29] M. Vila, V. Sunko, and J. E. Moore, Orbital-spin locking and its optical signatures in altermagnets, *Phys. Rev. B* **112**, L020401 (2025).
- [30] Q. N. Meier, A. Carta, C. Ederer, and A. Cano, (anti-) altermagnetism from orbital ordering in the Ruddlesden-Popper chromates $\text{Sr}_{n+1}\text{Cr}_n\text{O}_{3n+1}$, *arXiv:2502.01515* (2025).
- [31] C. Wu and S.-C. Zhang, Dynamic generation of spin-orbit coupling, *Phys. Rev. Lett.* **93**, 036403 (2004).
- [32] C. Wu, K. Sun, E. Fradkin, and S.-C. Zhang, Fermi liquid instabilities in the spin channel, *Phys. Rev. B* **75**, 115103 (2007).
- [33] T. Jungwirth, R. M. Fernandes, E. Fradkin, A. H. MacDonald, J. Sinova, and L. Šmejkal, Altermagnetism: an unconventional spin-ordered phase of matter, *Newton* (2025).
- [34] Z. Qian, Y. Yang, S. Liu, and C. Wu, Fragile unconventional magnetism in RuO_2 by proximity to Landau-

- Pomeranchuk instability, *Phys. Rev. B* **111**, 174425 (2025).
- [35] X. Zhu, X. Huo, S. Feng, S.-B. Zhang, S. A. Yang, and H. Guo, Design of altermagnetic models from spin clusters, *Phys. Rev. Lett.* **134**, 166701 (2025).
- [36] J. Krempaský, L. Šmejkal, S. W. D'Souza, M. Hajlaoui, G. Springholz, K. Uhlířová, F. Alarab, P. C. Constantinou, V. Strocov, D. Usanov, W. R. Pudelko, R. González-Hernández, A. Birk Hellenes, Z. Jansa, H. Reichlová, Z. Šobán, R. D. Gonzalez Betancourt, P. Wadley, J. Sinova, D. Kriegner, J. Minár, J. H. Dil, and T. Jungwirth, Altermagnetic lifting of kramers spin degeneracy, *Nature* **626**, 517 (2024).
- [37] O. Fedchenko, J. Minár, A. Akashdeep, S. W. D'Souza, D. Vasilyev, O. Tkach, L. Odenbreit, Q. Nguyen, D. Kutnyakhov, N. Wind, L. Wenthau, M. Scholz, K. Rosnagel, M. Hoesch, M. Aeschlimann, B. Stadtmüller, M. Kläui, G. Schönhense, T. Jungwirth, A. B. Hellenes, G. Jakob, L. Šmejkal, J. Sinova, and H.-J. Elmers, Observation of time-reversal symmetry breaking in the band structure of altermagnetic RuO₂, *Science Advances* **10**, eadj4883 (2024).
- [38] S. Lee, S. Lee, S. Jung, J. Jung, D. Kim, Y. Lee, B. Seok, J. Kim, B. G. Park, L. Šmejkal, C.-J. Kang, and C. Kim, Broken kramers degeneracy in altermagnetic MnTe, *Phys. Rev. Lett.* **132**, 036702 (2024).
- [39] J. Ding, Z. Jiang, X. Chen, Z. Tao, Z. Liu, T. Li, J. Liu, J. Sun, J. Cheng, J. Liu, Y. Yang, R. Zhang, L. Deng, W. Jing, Y. Huang, Y. Shi, M. Ye, S. Qiao, Y. Wang, Y. Guo, D. Feng, and D. Shen, Large band splitting in *g*-wave altermagnet CrSb, *Phys. Rev. Lett.* **133**, 206401 (2024).
- [40] J. Liu, J. Zhan, T. Li, J. Liu, S. Cheng, Y. Shi, L. Deng, M. Zhang, C. Li, J. Ding, Q. Jiang, M. Ye, Z. Liu, Z. Jiang, S. Wang, Q. Li, Y. Xie, Y. Wang, S. Qiao, J. Wen, Y. Sun, and D. Shen, Absence of altermagnetic spin splitting character in rutile oxide RuO₂, *Phys. Rev. Lett.* **133**, 176401 (2024).
- [41] Z. Lin, D. Chen, W. Lu, X. Liang, S. Feng, K. Yamagami, J. Osiecki, M. Leandersson, B. Thiagarajan, J. Liu, C. Felser, and J. Ma, Observation of giant spin splitting and d-wave spin texture in room temperature altermagnet RuO₂, *arXiv:2402.04995* (2024).
- [42] B. Jiang, M. Hu, J. Bai, Z. Song, C. Mu, G. Qu, W. Li, W. Zhu, H. Pi, Z. Wei, Y.-J. Sun, Y. Huang, X. Zheng, Y. Peng, L. He, S. Li, J. Luo, Z. Li, G. Chen, H. Li, H. Weng, and T. Qian, A metallic room-temperature d-wave altermagnet, *Nat. Phys.* **21**, 754–759 (2025).
- [43] T. Osumi, S. Souma, T. Aoyama, K. Yamauchi, A. Honma, K. Nakayama, T. Takahashi, K. Ohgushi, and T. Sato, Observation of a giant band splitting in altermagnetic MnTe, *Phys. Rev. B* **109**, 115102 (2024).
- [44] J. Graham, T. Hicken, R. Regmi, M. Janoschek, I. Mazin, H. Luetkens, N. Ghimire, and Z. Guguchia, Local probe evidence supporting altermagnetism in Co_{1/4}NbSe₂, *arXiv:2503.09193* (2025).
- [45] H. Reichlova, R. Lopes Seeger, R. González-Hernández, I. Kounta, R. Schlitz, D. Kriegner, P. Ritzinger, M. Lammel, M. Leiviskä, A. Birk Hellenes, K. Olejník, V. Petříček, P. Doležal, L. Horak, E. Schmoranzero, A. Badura, S. Bertaina, A. Thomas, V. Baltz, L. Michez, J. Sinova, S. T. B. Goennenwein, T. Jungwirth, and L. Šmejkal, Observation of a spontaneous anomalous Hall response in the Mn₅Si₃ d-wave altermagnet candidate, *Nat. Commun.* **15**, 4961 (2024).
- [46] S. Reimers, L. Odenbreit, L. Šmejkal, V. N. Strocov, P. Constantinou, A. B. Hellenes, R. Jaeschke Ubierno, W. H. Campos, V. K. Bharadwaj, A. Chakraborty, T. Denneulin, W. Shi, R. E. Dunin-Borkowski, S. Das, M. Kläui, J. Sinova, and M. Jourdan, Direct observation of altermagnetic band splitting in CrSb thin films, *Nat. Commun.* **15**, 2116 (2024).
- [47] G. Yang, Z. Li, S. Yang, J. Li, H. Zheng, W. Zhu, Z. Pan, Y. Xu, S. Cao, W. Zhao, A. Jana, J. Zhang, M. Ye, Y. Song, L.-H. Hu, L. Yang, J. Fujii, I. Vobornik, M. Shi, H. Yuan, Y. Zhang, Y. Xu, and Y. Liu, Three-dimensional mapping of the altermagnetic spin splitting in CrSb, *Nature Communications* **16**, 1442 (2025).
- [48] A. Urru, D. Seleznev, Y. Teng, S. Y. Park, S. E. Reyes-Lillo, and K. M. Rabe, *G*-type antiferromagnetic BiFeO₃ is a multiferroic *g*-wave altermagnet, *Phys. Rev. B* **112**, 104411 (2025).
- [49] R. Chen, B. Zhou, and D.-H. Xu, Quasicrystalline altermagnetism, *arXiv:2507.18408* (2025).
- [50] Y. Li, M. Pan, J. Leng, Y. Chen, and H. Huang, Unconventional altermagnetism in quasicrystals: A hyperspatial projective construction, *arXiv:2508.01564* (2025).
- [51] Z.-Y. Shao, C. Lu, Z. Pan, Y.-B. Liu, and F. Yang, Classification of magnetism and altermagnetism in quasicrystals, *arXiv:2508.15702* (2025).
- [52] D. Levine and P. J. Steinhardt, Quasicrystals: A new class of ordered structures, *Phys. Rev. Lett.* **53**, 2477 (1984).
- [53] D. Levine and P. J. Steinhardt, Quasicrystals. i. definition and structure, *Phys. Rev. B* **34**, 596 (1986).
- [54] J. E. Socolar and P. J. Steinhardt, Quasicrystals. ii. unit-cell configurations, *Phys. Rev. B* **34**, 617 (1986).
- [55] S. Wessel, A. Jagannathan, and S. Haas, Quantum antiferromagnetism in quasicrystals, *Phys. Rev. Lett.* **90**, 177205 (2003).
- [56] Y. E. Kraus, Y. Lahini, Z. Ringel, M. Verbin, and O. Zeitlinger, Topological states and adiabatic pumping in quasicrystals, *Phys. Rev. Lett.* **109**, 106402 (2012).
- [57] S. Thiem and J. T. Chalker, Long-range magnetic order in models for rare-earth quasicrystals, *Phys. Rev. B* **92**, 224409 (2015).
- [58] E. C. Andrade, A. Jagannathan, E. Miranda, M. Vojta, and V. Dobrosavljević, Non-Fermi-liquid behavior in metallic quasicrystals with local magnetic moments, *Phys. Rev. Lett.* **115**, 036403 (2015).
- [59] J. Otsuki and H. Kusunose, Distributed hybridization model for quantum critical behavior in magnetic quasicrystals, *Journal of the Physical Society of Japan* **85**, 073712 (2016).
- [60] A. Koga and H. Tsunetsugu, Antiferromagnetic order in the Hubbard model on the Penrose lattice, *Phys. Rev. B* **96**, 214402 (2017).
- [61] H. Huang and F. Liu, Quantum spin Hall effect and spin bott index in a quasicrystal lattice, *Phys. Rev. Lett.* **121**, 126401 (2018).
- [62] H. Huang and F. Liu, Comparison of quantum spin Hall states in quasicrystals and crystals, *Phys. Rev. B* **100**, 085119 (2019).
- [63] S. Longhi, Topological phase transition in non-hermitian quasicrystals, *Phys. Rev. Lett.* **122**, 237601 (2019).
- [64] A. Koga, Superlattice structure in the antiferromagnetically ordered state in the Hubbard model on the

- Ammann-Beenker tiling, *Phys. Rev. B* **102**, 115125 (2020).
- [65] H. Miyazaki, T. Sugimoto, K. Morita, and T. Tohyama, Magnetic orders induced by RKKY interaction in Tsai-type quasicrystalline approximant Au-Al-Gd, *Phys. Rev. Mater.* **4**, 024417 (2020).
- [66] Y. Cao, Y. Zhang, Y.-B. Liu, C.-C. Liu, W.-Q. Chen, and F. Yang, Kohn-Luttinger mechanism driven exotic topological superconductivity on the Penrose lattice, *Phys. Rev. Lett.* **125**, 017002 (2020).
- [67] C. W. Duncan, S. Manna, and A. E. B. Nielsen, Topological models in rotationally symmetric quasicrystals, *Phys. Rev. B* **101**, 115413 (2020).
- [68] S. Manna, S. K. Das, and B. Roy, Noncrystalline topological superconductors, *Phys. Rev. B* **109**, 174512 (2024).
- [69] C.-B. Hua, Z.-R. Liu, T. Peng, R. Chen, D.-H. Xu, and B. Zhou, Disorder-induced chiral and helical Majorana edge modes in a two-dimensional Ammann-Beenker quasicrystal, *Phys. Rev. B* **104**, 155304 (2021).
- [70] T. Peng, C.-B. Hua, R. Chen, Z.-R. Liu, D.-H. Xu, and B. Zhou, Higher-order topological Anderson insulators in quasicrystals, *Phys. Rev. B* **104**, 245302 (2021).
- [71] R. Ghadimi, T. Sugimoto, K. Tanaka, and T. Tohyama, Topological superconductivity in quasicrystals, *Phys. Rev. B* **104**, 144511 (2021).
- [72] A. Koga, Antiferromagnetically ordered state in the half-filled Hubbard model on the socalar dodecagonal tiling, *Materials Transactions* **62**, 360 (2021).
- [73] C. Wang, F. Liu, and H. Huang, Effective model for fractional topological corner modes in quasicrystals, *Phys. Rev. Lett.* **129**, 056403 (2022).
- [74] A. Koga and S. Coates, Ferrimagnetically ordered states in the Hubbard model on the hexagonal golden-mean tiling, *Phys. Rev. B* **105**, 104410 (2022).
- [75] P. Ghosh, Exact quantum ground state of a two-dimensional quasicrystalline antiferromagnet, *Phys. Rev. B* **108**, 014426 (2023).
- [76] R. Chen, B. Zhou, and D.-H. Xu, Quasicrystalline second-order topological semimetals, *Phys. Rev. B* **108**, 195306 (2023).
- [77] Y.-B. Liu, J. Zhou, C. Wu, and F. Yang, Charge-4e superconductivity and chiral metal in 45°-twisted bilayer cuprates and related bilayers, *Nat. Commun.* **14**, 7926 (2023).
- [78] A. Uri, S. C. de la Barrera, M. T. Randeria, D. Rodan-Legrain, T. Devakul, P. J. D. Crowley, N. Paul, K. Watanabe, T. Taniguchi, R. Lifshitz, L. Fu, R. C. Ashoori, and P. Jarillo-Herrero, Superconductivity and strong interactions in a tunable moiré quasicrystal, *Nature* **620**, 762 (2023).
- [79] R. N. Araújo, C. C. Bellinati, and E. C. Andrade, Fragile magnetic order in metallic quasicrystals, *Phys. Rev. B* **110**, 165131 (2024).
- [80] Y.-B. Yang, J.-H. Wang, K. Li, and Y. Xu, Higher-order topological phases in crystalline and non-crystalline systems: a review, *Journal of Physics: Condensed Matter* **36**, 283002 (2024).
- [81] Y.-B. Liu, J. Zhou, and F. Yang, Nematic superconductivity and its critical vestigial phases in the quasicrystal, *Phys. Rev. Lett.* **133**, 136002 (2024).
- [82] L. Liu, Z.-X. Li, and F. Yang, Superconductivity and charge density wave in the Holstein model on the Penrose lattice, *Phys. Rev. Lett.* **134**, 206001 (2025).
- [83] A. Jagannathan and T. Jolicoeur, Entropic selection of magnetization in a frustrated two-dimensional magnetic model, *Phys. Rev. B* **111**, 054409 (2025).
- [84] A. Jagannathan, Missing link between the two-dimensional quantum Hall problem and one-dimensional quasicrystals, *Phys. Rev. B* **112**, L100102 (2025).
- [85] Y. Wang, G. Rai, C. Matsumura, A. Jagannathan, and S. Haas, Superconductivity in the Fibonacci chain, *Phys. Rev. B* **109**, 214507 (2024).
- [86] L.-Q. Xia, A. Uri, J. Yan, A. Sharpe, F. Gaggioli, N. S. Ticea, J. May-Mann, K. Watanabe, T. Taniguchi, L. Fu, T. Devakul, J. H. Smet, and P. Jarillo-Herrero, Magic continuum in multi-moiré twisted trilayer graphene, [arXiv:2509.03583](https://arxiv.org/abs/2509.03583) (2025).
- [87] G. Sugiyama and S. Koonin, Auxiliary field monte-carlo for quantum many-body ground states, *Annals of Physics* **168**, 1 (1986).
- [88] S. Sorella, S. Baroni, R. Car, and M. Parrinello, A novel technique for the simulation of interacting fermion systems, *Europhysics Letters* **8**, 663 (1989).
- [89] S. Sorella, E. Tosatti, S. Baroni, R. Car, and M. Parrinello, Numerical simulation of the 1d and 2d Hubbard models: Fermi liquid behavior and its breakdown, *International Journal of Modern Physics B* **02**, 993 (1988).
- [90] See Supplementary Material at [URL], in which Sec. A defines the Hubbard model in the five QCs with their geometries, Sec. B provides principles and details of the non-uniform time-slice strategy in the PQMC algorithm, Sec.C provides different constructors of trial wavefunction, Sec. D give the expression of the spin-resolved angle-resolved photoemission spectrum weight, Sec. E and F exhibit more results and details under local and global magnetic pinning fields, respectively.
- [91] P. d'Ornellas, V. Leeb, A. G. Grushin, and J. Knolle, Altermagnetism without crystal symmetry, [arXiv:2504.08597](https://arxiv.org/abs/2504.08597) (2025).
- [92] D. Zhu, Z.-Y. Zhuang, Z. Wu, and Z. Yan, Topological superconductivity in two-dimensional altermagnetic metals, *Phys. Rev. B* **108**, 184505 (2023).
- [93] Y.-M. Wu, Y. Wang, and R. M. Fernandes, Intra-unit-cell singlet pairing mediated by altermagnetic fluctuations, *Phys. Rev. Lett.* **135**, 156001 (2025).
- [94] X. Ma, S. Wu, Z. Li, L. Hu, J. D. Dai, and C. Cao, Possible spin triplet pairing due to altermagnetic spin fluctuation, [arXiv:2509.09959](https://arxiv.org/abs/2509.09959) (2025).
- [95] C. Lu, C. Li, C. Cao, H. Yuan, F.-C. Zhang, and L.-H. Hu, Inter-orbital spin-triplet superconductivity from altermagnetic fluctuations, [arXiv:2510.19083](https://arxiv.org/abs/2510.19083) (2025).
- [96] J.-K. Bao, J.-Y. Liu, C.-W. Ma, Z.-H. Meng, Z.-T. Tang, Y.-L. Sun, H.-F. Zhai, H. Jiang, H. Bai, C.-M. Feng, Z.-A. Xu, and G.-H. Cao, Superconductivity in quasi-one-dimensional $k_2cr_3as_3$ with significant electron correlations, *Phys. Rev. X* **5**, 011013 (2015).
- [97] Y. Zhou, C. Cao, and F.-C. Zhang, Theory for superconductivity in alkali chromium arsenides $A_2Cr_3As_3$ ($a=k, rb, cs$), *Science Bulletin* **62**, 208 (2017).
- [98] X. Wu, F. Yang, C. Le, H. Fan, and J. Hu, Triplet p_z -wave pairing in quasi-one-dimensional $A_2Cr_3As_3$ superconductors ($A = K, Rb, Cs$), *Phys. Rev. B* **92**, 104511 (2015).
- [99] R. Y. Chen and N. L. Wang, Progress in Cr- and Mn-based superconductors: a key issues review, *Reports on Progress in Physics* **82**, 012503 (2018).

- [100] J. Yang, J. Luo, C. Yi, Y. Shi, Y. Zhou, and G. qing Zheng, Spin-triplet superconductivity in $K_2Cr_3As_3$, *Science Advances* **7**, eabl4432 (2021).
- [101] S. Ran, C. Eckberg, Q.-P. Ding, Y. Furukawa, T. Metz, S. R. Saha, I.-L. Liu, M. Zic, H. Kim, J. Paglione, and N. P. Butch, Nearly ferromagnetic spin-triplet superconductivity, *Science* **365**, 684 (2019).
- [102] L. Jiao, S. Howard, S. Ran, Z. Wang, J. O. Rodríguez, M. Sigrist, Z. Wang, N. P. Butch, and V. Madhavan, Chiral superconductivity in heavy-fermion metal UTe_2 , *Nature* **579**, 523 (2020).
- [103] I. M. Hayes, D. S. Wei, T. Metz, J. Zhang, Y. S. Eo, S. Ran, S. R. Saha, J. Collini, N. P. Butch, D. F. Agterberg, A. Kapitulnik, and J. Paglione, Multicomponent superconducting order parameter in UTe_2 , *Science* **373**, 797 (2021).
- [104] D. Aoki, J.-P. Brison, J. Flouquet, K. Ishida, G. Knebel, Y. Tokunaga, and Y. Yanase, Unconventional superconductivity in UTe_2 , *Journal of Physics: Condensed Matter* **34**, 243002 (2022).
- [105] S. K. Lewin, C. E. Frank, S. Ran, J. Paglione, and N. P. Butch, A review of UTe_2 at high magnetic fields, *Reports on Progress in Physics* **86**, 114501 (2023).
- [106] Y. Zhang, X. Luo, W. Feng, S. Tan, Q. Hao, Q. Zhang, D. Yuan, B. Wang, Y. Liu, Q. Liu, X. Wang, L. Luo, X. Zhu, Q. Chen, and X. Lai, Kondo entanglement in the quasi-two-dimensional heavy fermion compound $cesb_2$, *Phys. Rev. B* **106**, 045133 (2022).
- [107] O. P. Squire, S. A. Hodgson, J. Chen, V. Fedoseev, C. K. de Podesta, T. I. Weinberger, P. L. Alireza, and F. M. Grosche, Superconductivity beyond the conventional pauli limit in high-pressure $CeSb_2$, *Phys. Rev. Lett.* **131**, 026001 (2023).
- [108] Z. Shan, Y. Jiao, J. Guo, Y. Wang, J. Wu, J. Zhang, Y. Zhang, D. Su, D. T. Adroja, C. Balz, M. Gutmann, Y. Liu, H. Yuan, Z. Wang, Y. Song, and M. Smidman, Emergent ferromagnetic ladder excitations in heavy fermion superconductor $cesb_2$, *Phys. Rev. Lett.* **134**, 116704 (2025).
- [109] F. F. Assaad and I. F. Herbut, Pinning the order: The nature of quantum criticality in the Hubbard model on honeycomb lattice, *Phys. Rev. X* **3**, 031010 (2013).
- [110] F. Parisen Toldin, F. F. Assaad, and S. Wessel, Critical behavior in the presence of an order-parameter pinning field, *Phys. Rev. B* **95**, 014401 (2017).

SUPPLEMENTARY MATERIALS

A. Hubbard Model in Different Bipartite Quasicrystals

As the beginning of our study, we construct the Hubbard model in several 2D bipartite quasicrystals (QCs). The geometries of the five QCs we studied are shown in Fig. A1, including the D_4 symmetric Thue-Morse QC with central 8-site cluster in (a) panel, the D_4 symmetric Thue-Morse QC with central 4-site cluster in (b) panel, the D_2 symmetric Thue-Morse lattice in (c) panel, the D_5 symmetric Penrose QC in (d) panel and the D_8 symmetric Ammann-Beenker lattice in (e) panel.

The Hubbard Hamiltonian in the D_4 and D_2 symmetric Thue-Morse lattices takes the form of

$$H = -t_1 \sum_{\langle i,j \rangle \sigma} \left(c_{i\sigma}^\dagger c_{j\sigma} + \text{h.c.} \right) - t_2 \sum_{\langle\langle i,j \rangle\rangle \sigma} \left(c_{i\sigma}^\dagger c_{j\sigma} + \text{h.c.} \right) + U \sum_i n_{i\uparrow} n_{i\downarrow}, \quad (S1)$$

and the one in the D_5 symmetric Penrose lattice and D_8 symmetric Ammann-Beenker lattice is written as

$$H = -t_1 \sum_{\langle i,j \rangle \sigma} \left(c_{i\sigma}^\dagger c_{j\sigma} + \text{h.c.} \right) + U \sum_i n_{i\uparrow} n_{i\downarrow}. \quad (S2)$$

Here, $\langle i, j \rangle$ and $\langle\langle i, j \rangle\rangle$ denote the nearest neighbor (NN) and the next nearest neighbor (NNN), respectively. $c_{i\sigma}^{(\dagger)}$ annihilates (creates) a spin- σ electron at site i and $n_{i\sigma}$ denotes the number operator for spin- σ electrons at site i . We set $t_1 = 1$, $t_2 = 0.5$ and $U = 4$ throughout this work.

B. Projector Quantum Monte Carlo Algorithm with Non-uniform Time Slice Strategy

In this section, we propose a non-uniform time slice strategy applicable to the projector quantum Monte Carlo (PQMC) algorithm, which saves more than 40% of time with the same accuracy compared to the usual uniform time slice strategy.

In PQMC simulations, the expectation of a physical quantity O is written as

$$\langle O \rangle = \lim_{\Theta \rightarrow \infty} \frac{\langle \psi | e^{-\Theta H} O e^{-\Theta H} | \psi \rangle}{\langle \psi | e^{-2\Theta H} | \psi \rangle}, \quad (S3)$$

where $|\psi\rangle$ represents the trial wave function. Θ denotes the total imaginary time, and $e^{-\Theta H}$ is the total imaginary time projection operator. The overlap integral between the ground state and the trial wave function $|\langle \Psi_0 | \psi \rangle|^2$ can

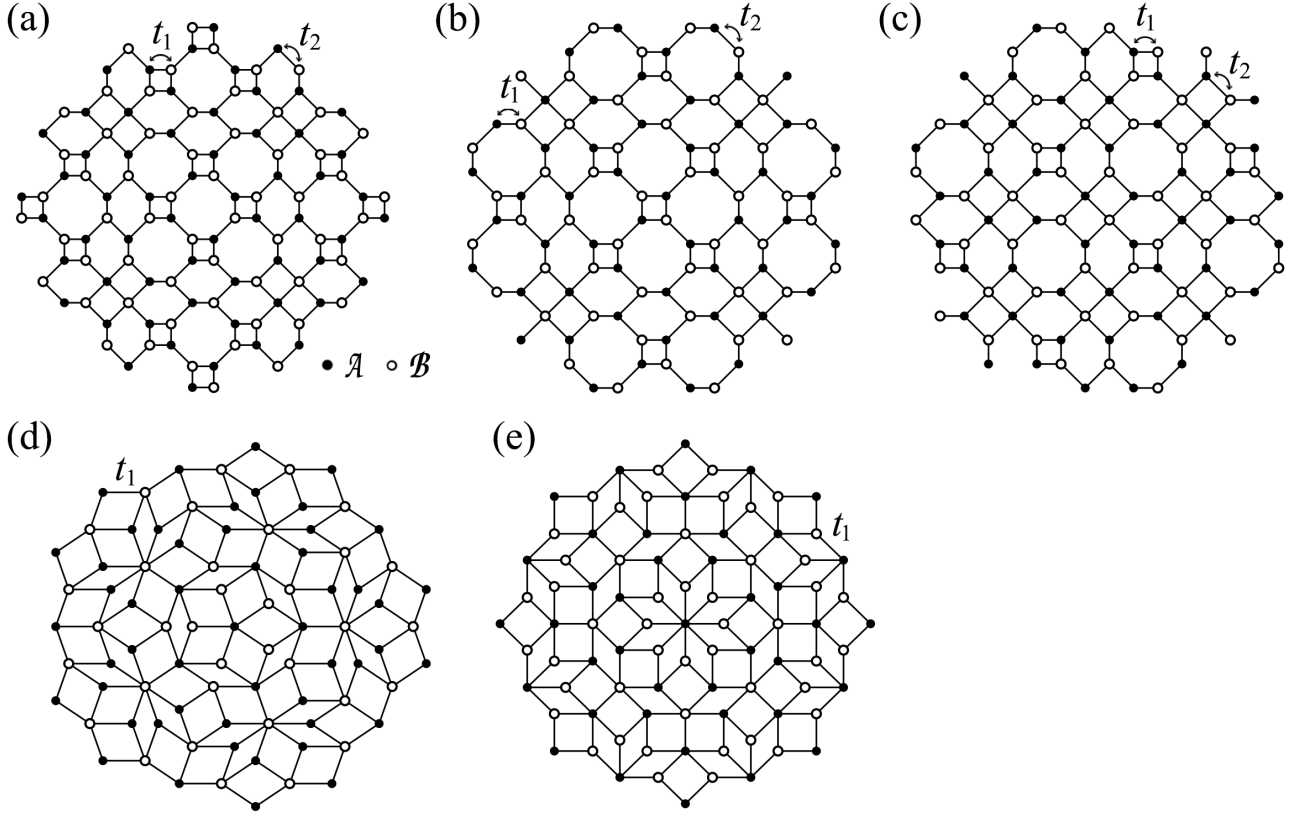


FIG. A1. (a-e) The schematic diagram of D_4 symmetric Thue-Morse lattice with central 8-site cluster for (a), D_4 symmetric Thue-Morse lattice with central 4-site cluster for (b), D_2 symmetric Thue-Morse lattice for (c), D_5 symmetric Penrose lattice for (d) and D_8 symmetric Ammann-Beenker lattice for (e). The solid (hollow) circle denotes the site in sublattice \mathcal{A} (\mathcal{B}) and the solid line represents the NN or NNN bond.

depict the degree of approximation between the two. $|\langle \Psi_0 | \psi \rangle|^2 = 1$ indicates that the trial wave function is the exact ground state, while $|\langle \Psi_0 | \psi \rangle|^2 = 0$ implies that the two are orthogonal. As it gets closer to 0, the larger Θ is required to project the trial wave function to reach the ground state.

For systems with many-body interactions, the Hubbard-Stratonovich (HS) decomposition is used to deal with the interaction terms, in which the total projection operator $e^{-2\Theta H}$ is decomposed into projection operators with several time slices as

$$e^{-2\Theta H} = \lim_{n \rightarrow \infty} e^{-2n\Delta\tau H}, \quad (\text{S4})$$

which is always implemented numerically using the Trotter decomposition and thus introduce the so-called Trotter error. Obviously, the accuracy of the simulated ground state with the same total imaginary time Θ is restricted by both the deviation of the trial wave function from the exact ground state and the Trotter error. When the overlap integral is less than a certain threshold, the deviation of the trial wave function from the exact ground state cannot be adequately eliminated after projection; while the time slices $\Delta\tau$ are too large, the Trotter error leads to insufficient simulation accuracy. When both are taken into account, the excessive number of time slices limits the computational efficiency of PQMC simulations.

In previous PQMC studies, the time slices $\Delta\tau$ are set to a unitary value, leading to a large number of time slices $\Delta\tau$ for a sufficiently large Θ and a sufficiently small Trotter error. Here, we propose a non-uniform time-slice strategy to accelerate the PQMC simulation by setting a series of different $\Delta\tau$. The strategy decomposes the total projection operator into projection operators with non-uniform time slices as

$$e^{-\Theta H} O e^{-\Theta H} = \lim_{n \rightarrow \infty} e^{-\Delta\tau_1 H} e^{-\Delta\tau_2 H} \dots e^{-\Delta\tau_n H} O e^{-\Delta\tau_n H} e^{-\Delta\tau_{n-1} H} \dots e^{-\Delta\tau_1 H}, \quad (\text{S5})$$

$$e^{-2\Theta H} = \lim_{n \rightarrow \infty} e^{-\Delta\tau_1 H} e^{-\Delta\tau_2 H} \dots e^{-\Delta\tau_n H} e^{-\Delta\tau_n H} e^{-\Delta\tau_{n-1} H} \dots e^{-\Delta\tau_1 H}, \quad (\text{S6})$$

where

$$\Theta = \sum_{i=1}^n \Delta\tau_i \quad \text{and} \quad \Delta\tau_1 \geq \Delta\tau_2 \geq \dots \geq \Delta\tau_n > 0. \quad (\text{S7})$$

This strategy aims to balance the Trotter error and the error between the trial wave function and the exact ground state by regulating the time slices. In a many-body system, particularly a strongly correlated system (e.g., large- U Hubbard model), the trial wave function $|\psi\rangle$ always deviates far from the exact ground state $|\Psi_0\rangle$, which requires a large Θ to cool $|\psi\rangle$ to $|\Psi_0\rangle$. Thus, it is a sensible strategy to preferentially apply the projection operator with larger time slices to the trial wave function for a rapid approach to the ground state, and then apply the ones with smaller time slices to reduce the Trotter error and further optimize the state.

In order to demonstrate the efficiency of the non-uniform strategy, we do a series of tests with the Hubbard model Eq. (S1) in the 8-site Thue-Morse lattice, while comparing with the results of exact diagonalization (ED). Fig. A2 (a) illustrates the geometry of the 8-site Thue-Morse lattice, where the solid lines indicate the NN or NNN bonds.

We solve the ground state for $2\Theta \approx 20$ with 600 non-uniform time slices, i.e., $2\Theta = 2 \times (20 \times 0.2 + 30 \times 0.1 + 30 \times 0.05 + 30 \times 0.02 + 50 \times 0.01 + 80 \times 0.005 + 60 \times 0.002) = 20.24$, compared to the results for $2\Theta = 20$ with unitary time slices $\Delta\tau = 0.01, 0.02$ and 0.04 and for $2\Theta = 30$ and 40 with unitary time slice $\Delta\tau = 0.01$.

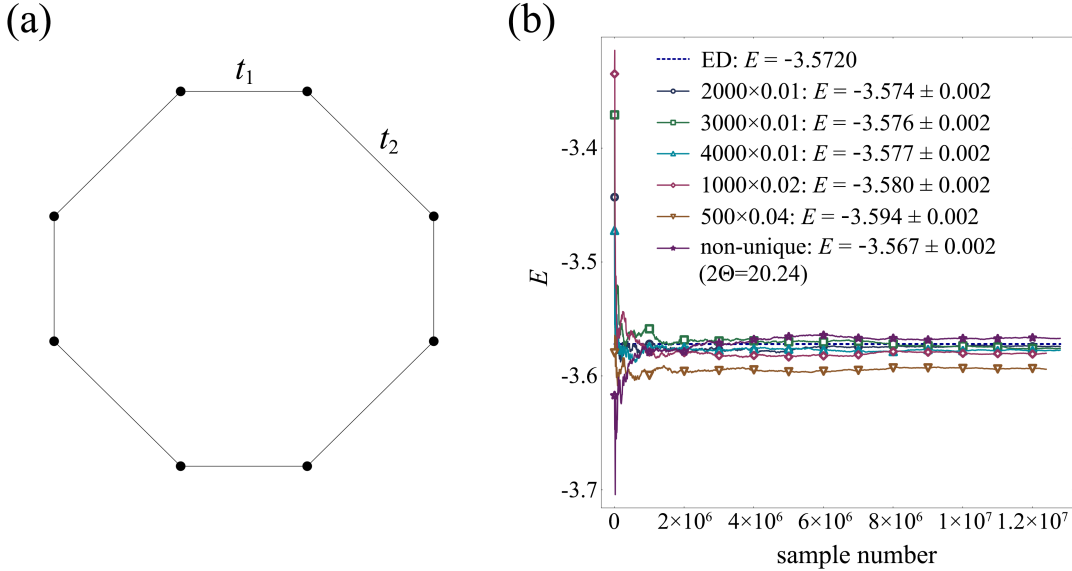


FIG. A2. (a) The schematic diagram of 8-site Thue-Morse lattice. The solid line represents the NN or NNN bond. (b) The energy as a function of sampling number. The exact ground state energy and the statistical mean and error of the energy for different parameters are labeled in the figure.

The results are shown in Fig. A2 (b). Comparison of results for $2\Theta = 20, 30$ and 40 with unitary time slices $\Delta\tau = 0.01$ indicates that $2\Theta = 20$ is sufficient to allow the trial wave function to evolve to the ground state, while the accumulated Trotter error amplifies the systematic error for $2\Theta = 30$ and 40 . Combining the results for $2\Theta = 20$ with uniform $\Delta\tau = 0.01, 0.02$ and 0.04 , it is easy to see that the increase in $\Delta\tau$ leads to a rapid deviation of the energy from the exact ground state due to the increasing Trotter error. The results of the non-uniform time slice strategy with 600 time slices demonstrate similar accuracy to the results for $2\Theta = 20$ with uniform $\Delta\tau = 0.02$, slightly worse than the one with $\Delta\tau = 0.01$. As a result, our non-uniform time slice strategy saves more than 40% of time with the same accuracy compared to the usual uniform time slice strategy, exhibiting a great value for numerate simulation.

In fact, we do not extensively test the performance of different sets of non-uniform time slices. We believe that more reasonable parameter selection allows this strategy to at least double the performance of the PQC algorithm, particularly in a strongly correlated system.

C. Trial wave function in the PQMC simulation

The trial wavefunction is introduced as the initial state for imaginary time propagation in PQMC simulations. For the half-filled Hubbard model, it is a common and convenient constructor of wave function as follows: We denote the tight-binding (TB) Hamiltonian (including hopping terms and pinning field terms) as H_{TB} , which can be decomposed to spin- \uparrow (H_{TB}^\uparrow) and spin- \downarrow (H_{TB}^\downarrow) components as $H_{\text{TB}} = H_{\text{TB}}^\uparrow + H_{\text{TB}}^\downarrow$. The coefficient matrix of H_{TB} is a block-diagonal matrix with H_{TB}^\uparrow and H_{TB}^\downarrow as diagonal blocks, i.e.,

$$[H_{\text{TB}}] = \begin{bmatrix} [H_{\text{TB}}^\uparrow] & \\ & [H_{\text{TB}}^\downarrow] \end{bmatrix}. \quad (\text{S8})$$

Here, $[\dots]$ denotes the coefficient matrix. Then we solve the eigen equations

$$[H_{\text{TB}}^\uparrow][\phi^\uparrow] \equiv [H_{\text{TB}}^\uparrow] \begin{bmatrix} \phi_{1,1}^\uparrow & \phi_{1,2}^\uparrow & \cdots & \phi_{1,n_\uparrow}^\uparrow \\ \phi_{2,1}^\uparrow & \phi_{2,2}^\uparrow & \cdots & \phi_{2,n_\uparrow}^\uparrow \\ \vdots & \vdots & \ddots & \vdots \\ \phi_{n,1}^\uparrow & \phi_{n,2}^\uparrow & \cdots & \phi_{n,n_\uparrow}^\uparrow \end{bmatrix} = \begin{bmatrix} \phi_{1,1}^\uparrow & \phi_{1,2}^\uparrow & \cdots & \phi_{1,n_\uparrow}^\uparrow \\ \phi_{2,1}^\uparrow & \phi_{2,2}^\uparrow & \cdots & \phi_{2,n_\uparrow}^\uparrow \\ \vdots & \vdots & \ddots & \vdots \\ \phi_{n,1}^\uparrow & \phi_{n,2}^\uparrow & \cdots & \phi_{n,n_\uparrow}^\uparrow \end{bmatrix} \begin{bmatrix} E_1^\uparrow & & & \\ & E_2^\uparrow & & \\ & & \ddots & \\ & & & E_{n_\uparrow}^\uparrow \end{bmatrix} \quad (\text{S9})$$

and

$$[H_{\text{TB}}^\downarrow][\phi^\downarrow] \equiv [H_{\text{TB}}^\downarrow] \begin{bmatrix} \phi_{1,1}^\downarrow & \phi_{1,2}^\downarrow & \cdots & \phi_{1,n_\downarrow}^\downarrow \\ \phi_{2,1}^\downarrow & \phi_{2,2}^\downarrow & \cdots & \phi_{2,n_\downarrow}^\downarrow \\ \vdots & \vdots & \ddots & \vdots \\ \phi_{n,1}^\downarrow & \phi_{n,2}^\downarrow & \cdots & \phi_{n,n_\downarrow}^\downarrow \end{bmatrix} = \begin{bmatrix} \phi_{1,1}^\downarrow & \phi_{1,2}^\downarrow & \cdots & \phi_{1,n_\downarrow}^\downarrow \\ \phi_{2,1}^\downarrow & \phi_{2,2}^\downarrow & \cdots & \phi_{2,n_\downarrow}^\downarrow \\ \vdots & \vdots & \ddots & \vdots \\ \phi_{n,1}^\downarrow & \phi_{n,2}^\downarrow & \cdots & \phi_{n,n_\downarrow}^\downarrow \end{bmatrix} \begin{bmatrix} E_1^\downarrow & & & \\ & E_2^\downarrow & & \\ & & \ddots & \\ & & & E_{n_\downarrow}^\downarrow \end{bmatrix}, \quad (\text{S10})$$

where n denotes the number of lattice sites and $n_\uparrow = \frac{n}{2}$ ($n_\downarrow = \frac{n}{2}$) denotes the particle number of spin- \uparrow (spin- \downarrow) Fermion. E_i^\uparrow (E_i^\downarrow) is the i -th lowest eigenvalue of H_{TB}^\uparrow (H_{TB}^\downarrow) with the eigenvector ϕ_i^\uparrow (ϕ_i^\downarrow) whose coefficient matrix is the i -th column of $[\phi^\uparrow]$ ($[\phi^\downarrow]$).

We construct the trial wave function $|\psi\rangle$ as

$$|\psi\rangle = \prod_{m=1}^{N/2} \prod_{\sigma} \sum_{i=1}^N \phi_{im}^\sigma c_{i\sigma}^\dagger |0\rangle, \quad (\text{S11})$$

with the coefficient matrix

$$[\psi] = \begin{bmatrix} [\phi^\uparrow] & \\ & [\phi^\downarrow] \end{bmatrix} = \begin{bmatrix} \phi_{1,1}^\uparrow & \phi_{1,2}^\uparrow & \cdots & \phi_{1,n_\uparrow}^\uparrow & & & \\ \phi_{2,1}^\uparrow & \phi_{2,2}^\uparrow & \cdots & \phi_{2,n_\uparrow}^\uparrow & & & \\ \vdots & \vdots & \ddots & \vdots & & & \\ \phi_{n,1}^\uparrow & \phi_{n,2}^\uparrow & \cdots & \phi_{n,n_\uparrow}^\uparrow & & & \\ & & & & \phi_{1,1}^\downarrow & \phi_{1,2}^\downarrow & \cdots & \phi_{1,n_\downarrow}^\downarrow \\ & & & & \phi_{2,1}^\downarrow & \phi_{2,2}^\downarrow & \cdots & \phi_{2,n_\downarrow}^\downarrow \\ & & & & \vdots & \vdots & \ddots & \vdots \\ & & & & \phi_{n,1}^\downarrow & \phi_{n,2}^\downarrow & \cdots & \phi_{n,n_\downarrow}^\downarrow \end{bmatrix}. \quad (\text{S12})$$

The constructor is sign-problem-free in the lattice with a gapped Fermi surface (e.g. D_2 and D_4 symmetric Thue-Morse lattice). However, the sign-problem occurs in the half-filling Hubbard model with a gapless ground state of H_{TB} (e.g. D_5 symmetric Penrose lattice or D_8 symmetric Ammann-Beenker lattice) because of the incompleteness of the trial wave function (S11), which can be avoided by the particle-hole (PH) transformation.

Another character of the trial wave function (S11) is the fixed and equal particle numbers of spin- \uparrow and spin- \downarrow , which requires that the net magnetism of the measured ground state be zero. Without the magnetic pinning field, the spin SU(2) symmetry preserves the measured ground state with zero net magnetism in finite size. However, the introduction of magnetic pinning field explicitly breaks spin SU(2) and \mathcal{T} symmetries, leading to a possible non-zero

net magnetism and the particle number difference $\langle n_\uparrow \rangle - \langle n_\downarrow \rangle$ that cannot be determined a priori. Therefore, we propose a new and complete constructor to capture different Néel order, which avoids the sign-problem without the aid of PH transformation.

We denote the TB Hamiltonian without pinning field as $H_{\text{TB}0} = H_{\text{TB}0}^\uparrow + H_{\text{TB}0}^\downarrow$, where H_{K0}^\uparrow (H_{K0}^\downarrow) is the spin- \uparrow (spin- \downarrow) component. The coefficient matrix follows

$$[H_{\text{TB}0}] = \begin{bmatrix} [H_{\text{TB}0}^\uparrow] \\ [H_{\text{TB}0}^\downarrow] \end{bmatrix}. \quad (\text{S13})$$

Here, $[H_{\text{TB}0}^\uparrow] = [H_{\text{TB}0}^\downarrow]$. Different from Eqs (S9) and (S10), the eigen equations are solved by

$$[H_{\text{TB}0}^\sigma][\phi] \equiv [H_{\text{TB}0}^\sigma] \begin{bmatrix} \phi_{1,1} & \phi_{1,2} & \cdots & \phi_{1,n} \\ \phi_{2,1} & \phi_{2,2} & \cdots & \phi_{2,n} \\ \vdots & \vdots & \ddots & \vdots \\ \phi_{n,1} & \phi_{n,2} & \cdots & \phi_{n,n} \end{bmatrix} = \begin{bmatrix} \phi_{1,1} & \phi_{1,2} & \cdots & \phi_{1,n} \\ \phi_{2,1} & \phi_{2,2} & \cdots & \phi_{2,n} \\ \vdots & \vdots & \ddots & \vdots \\ \phi_{n,1} & \phi_{n,2} & \cdots & \phi_{n,n} \end{bmatrix} \begin{bmatrix} E_1 & & & \\ & E_2 & & \\ & & \ddots & \\ & & & E_n \end{bmatrix}. \quad (\text{S14})$$

The trial wave function $|\psi\rangle$ are constructed by

$$|\psi\rangle = \prod_{m=1}^N \sum_{i=1}^N \phi_{im} (c_{i\uparrow}^\dagger + c_{i\downarrow}^\dagger) |0\rangle, \quad (\text{S15})$$

with the coefficient matrix

$$[\psi] = \begin{bmatrix} \phi_{1,1} & \phi_{1,2} & \cdots & \phi_{1,n} \\ \phi_{2,1} & \phi_{2,2} & \cdots & \phi_{2,n} \\ \vdots & \vdots & \ddots & \vdots \\ \phi_{n,1} & \phi_{n,2} & \cdots & \phi_{n,n} \\ \phi_{1,1} & \phi_{1,2} & \cdots & \phi_{1,n} \\ \phi_{2,1} & \phi_{2,2} & \cdots & \phi_{2,n} \\ \vdots & \vdots & \ddots & \vdots \\ \phi_{n,1} & \phi_{n,2} & \cdots & \phi_{n,n} \end{bmatrix}. \quad (\text{S16})$$

In our subsequent study, we confirm the existence of altermagnetism (AM) and antiferromagnetism (AFM) Néel order with a zero net magnetism in D_4 and D_2 symmetric Thue-Morse lattice using the trial wave function (S15). As a result, we reconsider the trial wave function (S11) to accelerate the simulations.

D. Spin-Resolved Angle-Resolved Photoemission Spectrum

To distinguish the AM and AFM states, we consider the spin-resolved angle-resolved photoemission spectrum.

We begin with a mean-field Hamiltonian with magnetic order,

$$H_{\text{MF}} = -t_1 \sum_{\langle i,j \rangle \sigma} (c_{i\sigma}^\dagger c_{j\sigma} + \text{h.c.}) - t_2 \sum_{\langle\langle i,j \rangle\rangle \sigma} (c_{i\sigma}^\dagger c_{j\sigma} + \text{h.c.}) - \mu \sum_{i\sigma} n_{i\sigma} - \frac{2U}{3} \sum_i \langle S_i^z \rangle (n_{i\uparrow} - n_{i\downarrow}). \quad (\text{S17})$$

For Thue-Morse lattice, $t_1 = 1$ and $t_2 = 0.5$. In the Wannier basis, the matrix form of H_{MF} is block-diagonal,

$$[H_{\text{MF}}] = \begin{bmatrix} [H_\uparrow] \\ [H_\downarrow] \end{bmatrix}, \quad (\text{S18})$$

where $[H_{\text{MF}}]$ is the matrix form of H_{MF} in the Wannier basis, and $[H_\sigma]$ is the matrix form of the mean-field Hamiltonian for spin σ , which is defined as

$$H_\sigma = -t_1 \sum_{\langle i,j \rangle} (c_{i\sigma}^\dagger c_{j\sigma} + \text{h.c.}) - t_2 \sum_{\langle\langle i,j \rangle\rangle} (c_{i\sigma}^\dagger c_{j\sigma} + \text{h.c.}) - \mu \sum_i n_{i\sigma} - \frac{2U}{3} \sigma \sum_i \langle S_i^z \rangle n_{i\sigma}. \quad (\text{S19})$$

The spectrum weight for spin σ at a certain energy level ω is expressed as

$$\mathcal{A}_\sigma(\mathbf{p}, \omega) = -\frac{\eta}{\pi} \frac{|\langle \mathbf{p}\sigma | m\sigma \rangle|^2}{(\omega - E_m^\sigma)^2 + \eta^2}, \quad (\text{S20})$$

where E_m^σ and $|m\sigma\rangle$ are the m -th eigenvalue and the corresponding eigenstate of H_σ , $|\mathbf{p}\sigma\rangle = \frac{1}{\sqrt{N}} \sum_i e^{i\mathbf{p}\cdot\mathbf{r}_i} c_{i\sigma}^\dagger |0\rangle$ (N is the number of sites, \mathbf{r}_i is the position of site i and $|0\rangle$ is vacuum state) is the plane wave with momentum \mathbf{p} , and η is a small Lorentzian expansion width.

E. More Details and Results with Local Magnetic Pinning Field

The PQMC algorithm is limited by the inability to distinguish between degenerate ground states, and therefore cannot correctly compute the nonzero order parameters for spontaneous symmetry breaking. In addition, the correlation function cannot accurately evaluate the magnitude of the local order parameters for further spectroscopic study. Therefore, we introduce the pinning field and obtain the exact magnitude and distribution of the order parameters by extrapolation within the linear response region.

In this section, we apply the local magnetic pinning field of different patterns on the central small-cluster or single-site to determine the pattern of the ground state. The local magnetic pinning field is written as

$$H_p^{\text{local}} = h_l \sum_{i \in \mathcal{C}} \text{sign}(i) S_i^z, \quad (\text{S21})$$

where \mathcal{C} represents the central small-cluster or single-site and $\text{sign}(i)$ denotes the sign of the pinning field at the site i . S_i^z is the z -component spin operator at site i . The total Hamiltonian is written as

$$H = -t_1 \sum_{\langle i,j \rangle \sigma} (c_{i\sigma}^\dagger c_{j\sigma} + \text{h.c.}) - t_2 \sum_{\langle\langle i,j \rangle\rangle \sigma} (c_{i\sigma}^\dagger c_{j\sigma} + \text{h.c.}) + U \sum_i n_{i\uparrow} n_{i\downarrow} + H_p^{\text{local}}. \quad (\text{S22})$$

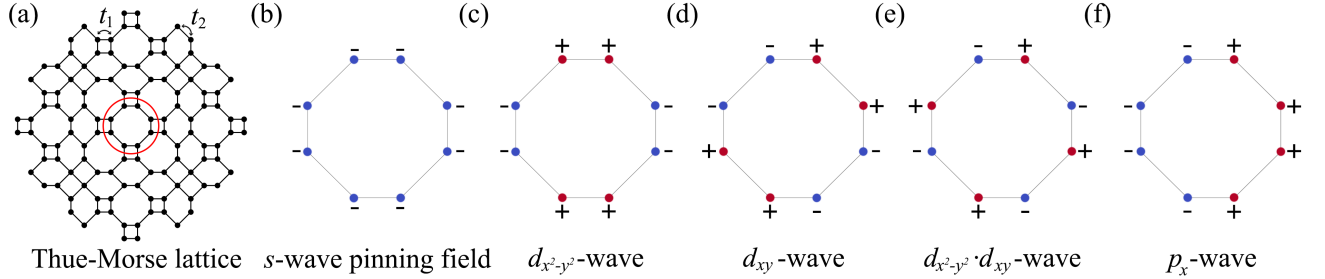


FIG. A3. (a) The schematic diagram of 120-site D_4 symmetric Thue-Morse lattice with central 8-site cluster circled in red. The black dot denotes the site and the solid line represents the NN or NNN bond. The local magnetic pinning field is applied in the cluster circled in red. (b-f) The schematic diagram of the local magnetic pinning field signs of s -wave for (b), $d_{x^2-y^2}$ -wave for (c), d_{xy} -wave for (d), $d_{x^2-y^2} \cdot d_{xy}$ -wave for (e), p_x -wave pattern for (f).

Here, we take the D_4 symmetric Thue-Morse lattice with central 8-site cluster as an example. Fig. A3 (a) exhibits the structure of 120-site D_4 symmetric Thue-Morse lattice with central 8-site cluster circled in red, where the black dot represents the site and the solid line represents the NN or NNN bond. Figs. A3 (b-f) show the signs of the local magnetic pinning field with s -wave, $d_{x^2-y^2}$ -wave, d_{xy} -wave, $d_{x^2-y^2} \cdot d_{xy}$ -wave, p_x -wave pattern, respectively. We set $t_1 = 1$, $t_2 = 0.5$, $U = 4$ and $h_l = 0.2$ to determine the ground state pattern of the original Hamiltonian (S1) without the pinning field.

Fig. A4 shows the results under local pinning field with different patterns. As shown in Fig. A4 (a), the ground state of the Hamiltonian (S22) with the local magnetic pinning field with $d_{x^2-y^2} \cdot d_{xy}$ pattern holds the lowest energy. As the introduction of a weak local pinning field lifts the energy of the ground state mismatching the pattern of the pinning field and lowers the matched one, the results indicate that the ground state of the original Hamiltonian (S1) without the pinning field takes $d_{x^2-y^2} \cdot d_{xy}$ pattern.

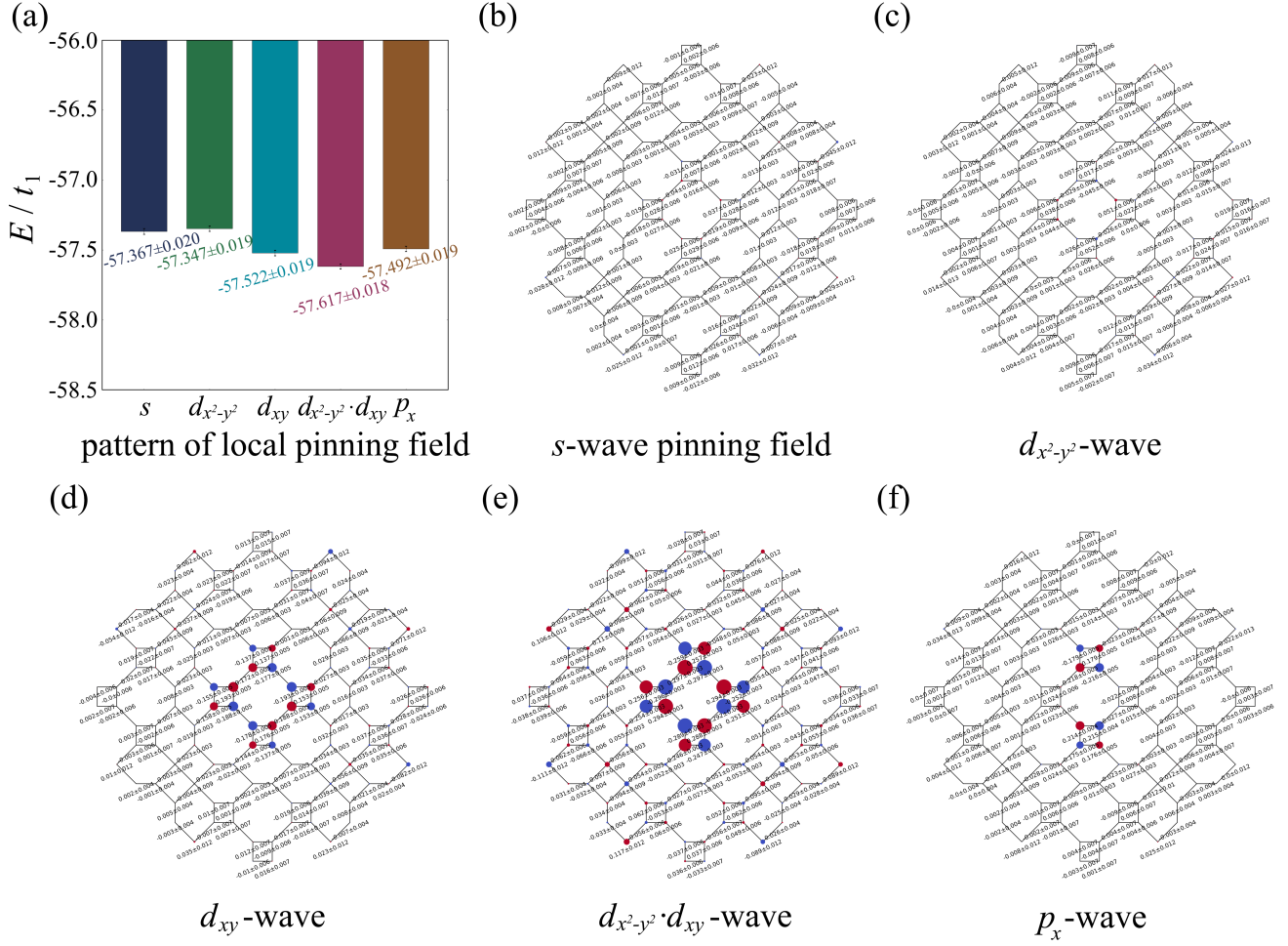


FIG. A4. (a) The ground state energies in the D_4 symmetric Thue-Morse lattice with under local magnetic pinning fields with different patterns on the central 8-site cluster. (b-f) The distribution of the magnetic order parameter $\langle S_i^z \rangle$ under local magnetic pinning fields with s -wave for (b), $d_{x^2-y^2}$ -wave for (c), d_{xy} -wave for (d), $d_{x^2-y^2} \cdot d_{xy}$ -wave for (e), p_x -wave pattern for (f). The values of $\langle S_i^z \rangle$ are labeled in the figure.

Figs. A4 (b-f) exhibit the distribution of the magnetic order parameter $\langle S_i^z \rangle$ under local magnetic pinning fields with s -wave, $d_{x^2-y^2}$ -wave, d_{xy} -wave, $d_{x^2-y^2} \cdot d_{xy}$ -wave, p_x -wave pattern, respectively. The results indicate that the order parameter $\langle S_i^z \rangle$ under the pinning field with $d_{x^2-y^2} \cdot d_{xy}$ pattern maintains a finite value within the finite size, while the ones under the pinning fields with other patterns quickly fall to zero with the increasing distance from the central cluster. Since the effect of a local pinning field decays algebraically with distance[109, 110], a weak mismatched local pinning field can only pin the local order parameter, while the matched one can stabilize the global order parameter by the existence of the long-range order. The behavior of the distribution of the magnetic order parameter $\langle S_i^z \rangle$ in finite size also suggests that the ground state of the original Hamiltonian (S1) without the pinning field holds the $d_{x^2-y^2} \cdot d_{xy}$ -wave pattern.

In short, both the lowest energy and the finite value of $\langle S_i^z \rangle$ in finite size indicate that $d_{x^2-y^2} \cdot d_{xy}$ -wave is the ground state pattern of the original Hamiltonian (S1) without the pinning field.

Similarly, we investigate the ground state properties of different QCs under the corresponding local pinning fields and determine their ground state patterns. Some of the results are shown in Fig. A5. Fig. A5 (a) exhibits that d_{xy} -wave is the pattern of local pinning field with the lowest ground state energy in the D_4 symmetric Thue-Morse lattice with central 4-site cluster, which also leads to a finite value of $\langle S_i^z \rangle$ in the finite size in Fig. A5 (b) in the same lattice, indicating that d_{xy} -wave is the pattern of the ground state of the original Hamiltonian (S1) without the pinning field. Fig. A5 (c) indicates that the distribution of $\langle S_i^z \rangle$ in the D_5 symmetric Penrose lattice maintains global symmetry breaking with the s -wave pattern, suggesting that the ground state pattern is s -wave, while Fig. A5 (d) implies the pattern in the D_8 symmetric lattice is s -wave as well. Figs. A5 (e-f) provide the similar information in

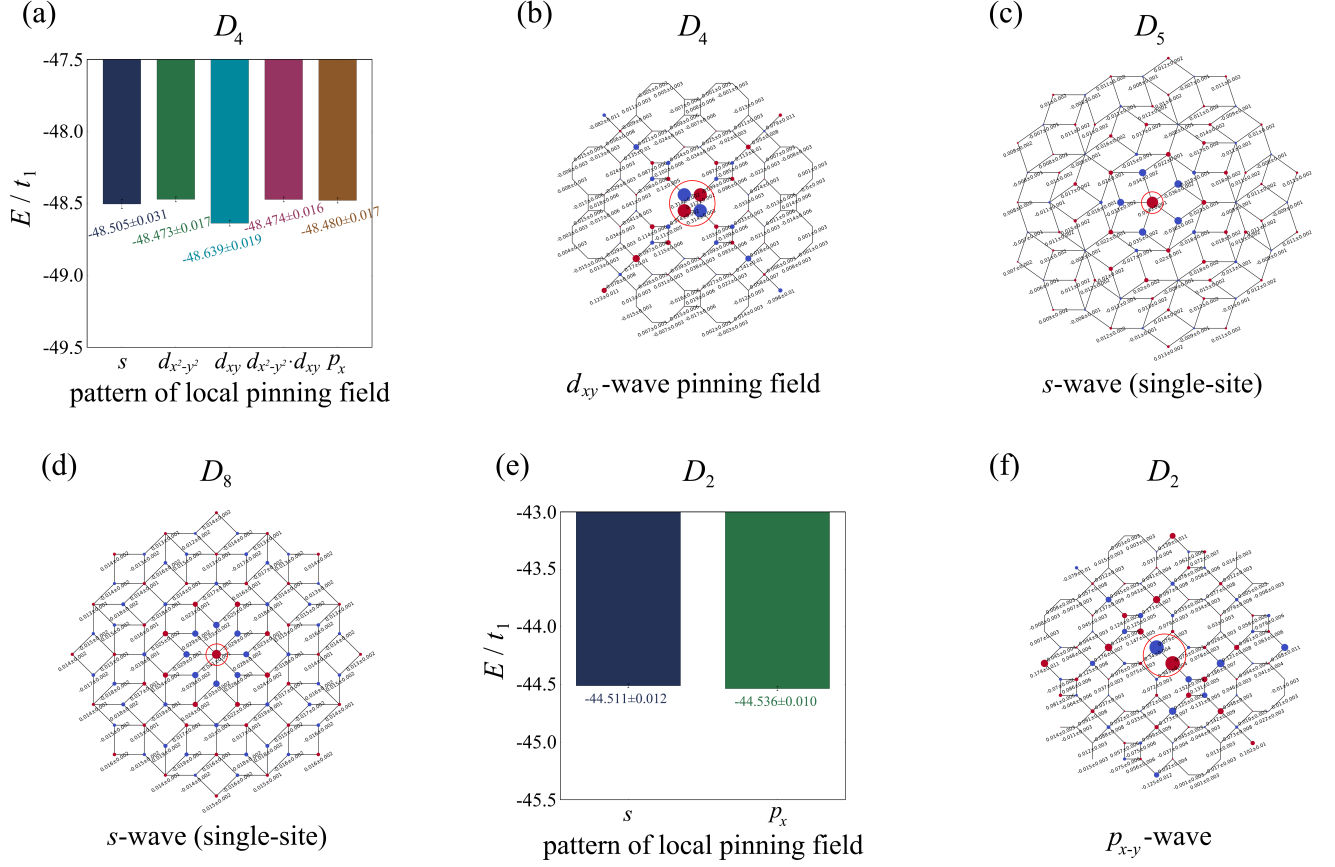


FIG. A5. (a) The ground state energies in the D_4 symmetric Thue-Morse lattice under local magnetic pinning fields with different patterns on the central 4-site cluster. (b) The distribution of the magnetic order parameter $\langle S_i^z \rangle$ under local magnetic pinning field with d_{xy} -wave (circled in red) in the D_4 symmetric lattice as same as (a). (c) The distribution of $\langle S_i^z \rangle$ under local pinning field at the central single-site (circled in red) in the D_5 symmetric lattice. (d) The distribution of $\langle S_i^z \rangle$ under local pinning field (circled in red) at the central single-site in the D_8 symmetric lattice. (e) The ground state energies in the D_2 symmetric Thue-Morse lattice under local magnetic pinning fields with different patterns on the central 2-site cluster. (f) The distribution of the magnetic order parameter $\langle S_i^z \rangle$ under local magnetic pinning field with p_{x-y} -wave (circled in red) in the D_2 symmetric lattice as same as (e). The values of $\langle S_i^z \rangle$ are labeled in the figure.

the D_2 symmetric Thue-Morse lattice, which demonstrates the ground state pattern is p_{x-y} -wave.

F. More Details and Results with Global Magnetic Pinning Field

At the end of Sec. E, we have obtained the ground state patterns in different QCs by the application of the local pinning field. Although the matched local pinning field globally maintains nonzero order parameters, the convergence rate at the lattice edge region is unsatisfactory with significant statistical error.

In this section, we introduce the global pinning fields with the same patterns as the ground states, which demonstrates better global convergence than the local one. The global pinning field is written as

$$H_p^{\text{global}} = h_g \sum_{i \in \mathcal{L}} \text{sign}(i) S_i^z, \quad (\text{S23})$$

where \mathcal{L} denotes the entire lattice. As all patterns determined in the different QCs take the form of the Néel order, we actually add the global pinning field with the same form in these bipartite lattices, i.e., one sublattice satisfies $\text{sign}(i) = 1$ and the other satisfies $\text{sign}(i) = -1$.

Here, we still take the D_4 symmetric Thue-Morse lattice with central 8-site cluster as an example, with the typical parameter set of $t_1 = 1$, $t_2 = 0.5$ and $U = 4$.

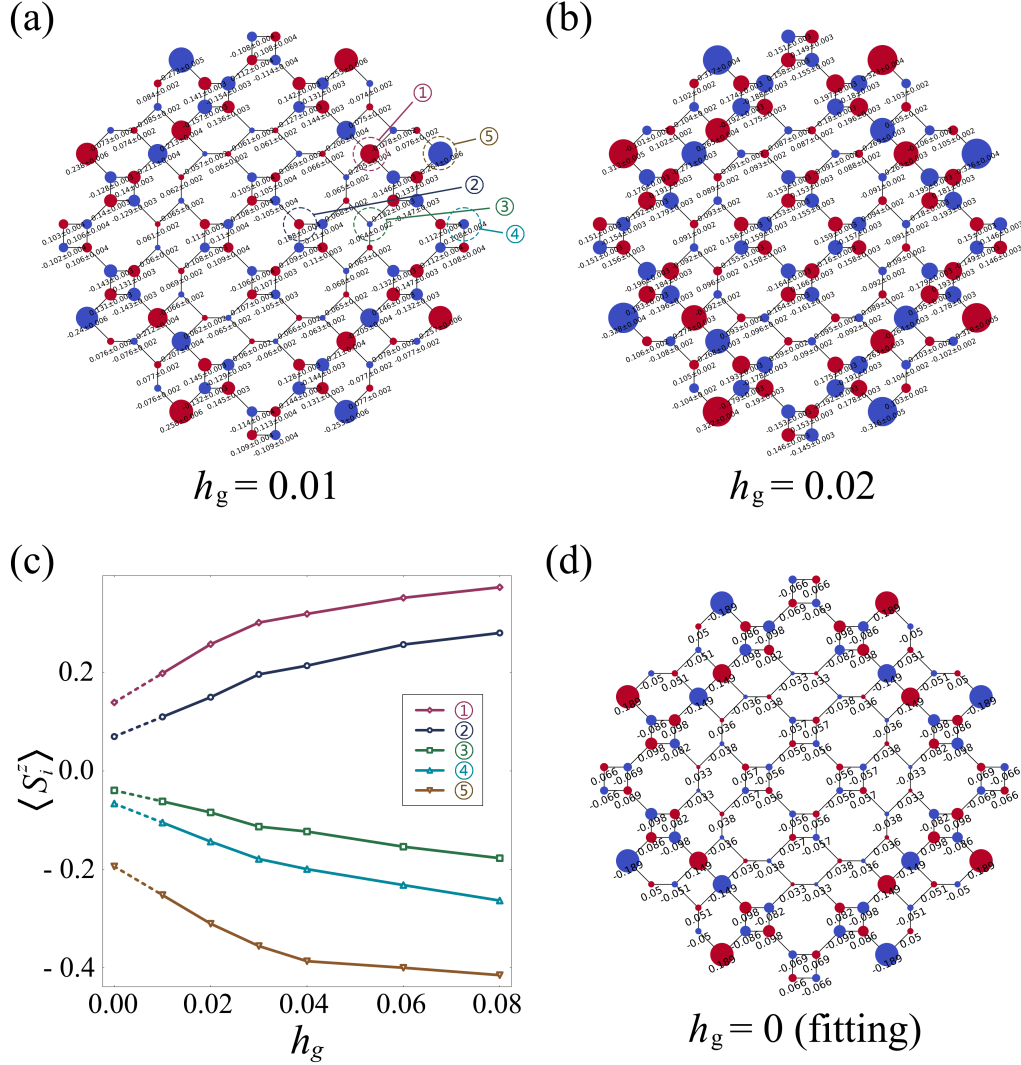


FIG. A6. (a-b) The distribution of the magnetic order parameter $\langle S_i^z \rangle$ under global magnetic pinning field $h_g = 0.01$ for (a) and $h_g = 0.02$ for (b). (c) The distribution of $\langle S_i^z \rangle$ as a function of the pinning field h_g at the sites i circled in (a). (d) The distribution of $\langle S_i^z \rangle$ fitted by the linear-fitting method. The values of $\langle S_i^z \rangle$ are labeled in the figure.

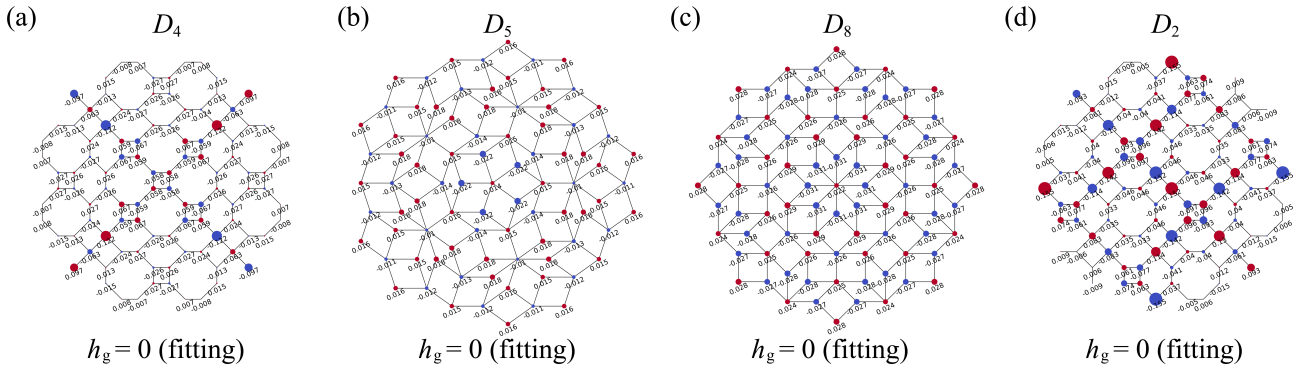


FIG. A7. (a-d) The distribution of $\langle S_i^z \rangle$ fitted by the linear-fitting method in the D_4 symmetric Thue-Morse lattice with central 4-site cluster for (a), D_5 symmetric lattice for (b), D_8 symmetry for (c) and D_2 symmetric Thue-Morse lattice for (d). The values of $\langle S_i^z \rangle$ are labeled in the figure.

We calculate the magnetic order parameter $\langle S_i^z \rangle$ under the global pinning fields of different strengths $h_g = 0.01, 0.02, 0.03, 0.04, 0.06$ and 0.08 . The results of $h_g = 0.01$ and 0.02 are shown in Figs. A6 (a) and (b), respectively, both of which show excellent global convergence with acceptable statistical error. Fig. A6 (c) illustrates the magnetic order parameter $\langle S_i^z \rangle$ as a function of the pinning field h_g at the sites i labeled in Fig. A6 (a). The results indicate that $\langle S_i^z \rangle$ exhibits a linear response behavior when $h_g < 0.03$, which allow us to obtain the actual distribution of $\langle S_i^z \rangle$ with $h_g = 0$ by the linear-fitting method. The fitting results after symmetrization with values are shown in Fig. A6 (d).

The fitting distributions of the magnetic order parameter $\langle S_i^z \rangle$ after symmetrization in other QCs are shown in Fig. A7.